



## Electron emission from CH<sub>4</sub> molecules in collisions with fast bare C ions

Anuvab Mandal,<sup>1</sup> Chandan Bagdia <sup>1</sup>, Madhusree Roy Chowdhury,<sup>1</sup> Shamik Bhattacharjee,<sup>1</sup> Deepankar Misra,<sup>1</sup>  
Juan M. Monti <sup>2</sup>, Roberto D. Rivarola,<sup>2</sup> and Lokesh C. Tribedi<sup>1,\*</sup>

<sup>1</sup>*Department of Nuclear and Atomic Physics, Tata Institute of Fundamental Research, 1 Homi Bhabha Road, Colaba, Mumbai 400005, India*

<sup>2</sup>*Instituto de Fisica Rosario (CONICET-UNR), Universidad Nacional de Rosario, 2000 Rosario, Argentina*



(Received 12 November 2019; revised manuscript received 7 March 2020; accepted 26 May 2020;  
published 17 June 2020; corrected 6 July 2020)

We present the energy and angular distributions of electron emission from a CH<sub>4</sub> molecule in collisions with fast bare C ions with energies 3.5 and 5.5 MeV/u. The absolute double differential cross sections (DDCS) are measured for the ejected electrons having energies from 11 eV to 330 eV for 3.5-MeV/u projectiles and from 5 eV to 330 eV for 5.5 MeV/u bare C ions. The emission is measured in the angular range from 20° to 160°. The forward-backward angular asymmetry, the single differential cross sections (SDCS), and the total cross section are deduced from the measured DDCS values. The energy and angular distributions of the DDCS and SDCS are compared with those calculated using a theoretical model based on the prior form of the continuum distorted wave–eikonal initial state (CDW-EIS) approximation. The dynamics of the process is considered within the CDW-EIS approximation, while the initial orbitals of the molecular target are represented using the complete neglect of the differential overlap approximation. The calculations are found to be in very good agreement with the measured cross sections. The angle dependence of the carbon K-LL Auger emission and the total Auger emission cross section are also derived for both projectile energies.

DOI: [10.1103/PhysRevA.101.062708](https://doi.org/10.1103/PhysRevA.101.062708)

### I. INTRODUCTION

Measurement of the double differential cross section (DDCS) ( $\frac{d^2\sigma}{d\Omega dE}$ ) of electron emission, as a function of the emitted electron energy  $E$  and the emission angle  $\theta$ , has importance in understanding the basic collision dynamics involving simple atoms as targets. The electron emission studies have been proved to be quite important in exploring the collision mechanisms in plasma physics, astrophysics, astrochemistry, and radiation biology. Moreover, such studies provide a stringent test of the validity of available theoretical frameworks.

Mostly, the smaller atomic and molecular targets with a few electrons have been the subject of experimental and theoretical investigations for a few decades. Different processes, such as the binary encounter (BE) mechanism, the two-center effect (TCE), and the soft-collision mechanism characterize the electron emission spectrum in such ion-atom or ion-molecule collisions. The TCE is known to influence the angular distribution of electron emission, in particular, the forward-backward angular asymmetry. This effect mainly depends on the perturbation strength  $q_p/v_p$ , where  $q_p$  and  $v_p$  are the charge state and the velocity of the projectile, respectively. The TCE has been studied for smaller atoms or molecules, such as H<sub>2</sub> [1–5], He [6,7], etc.

In recent years there has been increasing demand to study the interaction of ions with large molecules owing to a number of specific applications. A few examples are the radiation interaction with RNA/DNA base molecules, particularly in connection with hadron therapy [8–11], the UV absorption

in polycyclic aromatic hydrocarbon (PAH) molecules in interstellar space [12–18], and collective excitation in carbon-based nanoparticles, including fullerene [19–23], etc. These studies also require a better understanding of the ion collisions with smaller but multielectron molecules such as CH<sub>4</sub>, H<sub>2</sub>O etc. as references. In case of complicated molecular targets, the collision process is influenced by the multicenter nature of the target. The studies on such small molecules thus serve as an intermediate step to extend the model calculations for large biomolecules or PAH molecules.

Methane (CH<sub>4</sub>), the simplest hydrocarbon molecule, has a significant presence in both the interstellar medium and the solar system. It is one of the most abundant species in the atmospheres of many planets [24]. Moreover, to understand the electron emission from the PAH or DNA/RNA base molecules, the CH<sub>4</sub> plays an important role of a reference. There are several reports on the total ionization and electron capture studies for CH<sub>4</sub> in collisions with the protons as projectiles [25–35]. Several groups have also studied the dissociative ionization of CH<sub>4</sub> with protons [36–40], C and F ions [41] as projectiles.

Although there are few experimental [42,43] and theoretical [44,45] investigations on the electron emission in ionization of CH<sub>4</sub> upon electron and proton impact, such studies using fast heavy-ion projectiles is scarce [18,46]. Studies on heavy-ion collisions in general provide a stringent test to the theoretical models as the perturbation strength is large. For highly charged projectile ions, the electron emission mechanism is more complicated since the emitted electrons move under the influence of both the target nuclei and the projectile ions. The TCE is better described by theoretical models such as the continuum distorted wave–eikonal initial state (CDW-EIS), which takes into account the distortion of

\*lokesh@tifr.res.in

the electron wave function by the Coulomb potential of the incident projectile charge. This model, in general, describes the angular distribution of the e-DDCS and the forward-backward angular asymmetry well. However, a detailed investigation has revealed discrepancies between the calculated cross sections and the experimentally measured values even for simple targets such as H, H<sub>2</sub>, and He [1,6,47–50]. Apart from the TCE, the emitted electrons are also influenced due to the scattering from multicentered target nuclei. It is of interest to study the electron emission from a small molecule such as CH<sub>4</sub> and compare the results with a model calculation which takes care of the TCE as well as the molecular nature of the target.

In the present study we measure the DDCS of electron emission from the CH<sub>4</sub> molecule induced by 3.5 MeV/u and 5.5 MeV/u bare C ions. The absolute DDCS values are measured in the energy range from 11 eV to 330 eV for 3.5 MeV/u projectiles and in the energy range from 5 eV to 330 eV for 5.5 MeV/u projectiles. The DDCS is measured at emission angles ranging from 20° to 160°. Energy and angular distribution of electron emission and the forward-backward angular asymmetry are compared with the prior form of the CDW-EIS (CDW-EIS-prior) model calculations [51]. The single differential cross sections (SDCS) and the total cross section (TCS) are also calculated from the measured DDCS values and are compared with the CDW-EIS calculations.

## II. EXPERIMENTAL PROCEDURE

The details of the experimental technique are given elsewhere [52]. In brief, the bare C ion beam is obtained from the BARC-TIFR Pelletron accelerator at TIFR, Mumbai. The ion beam is collimated using a pair of four-jaw slits which are 1 meter apart from each other. An aperture of 4 mm diameter is used to collimate the ion beam to the interaction chamber that is kept at a base pressure of  $1 \times 10^{-7}$  mbar. The scattering chamber is flooded with CH<sub>4</sub> gas at a pressure of  $2 \times 10^{-4}$  mbar. The pressure is measured using a well-calibrated capacitance manometer (MKS Baratron). An electrically isolated Faraday cup is used for measuring the beam intensity from which the number of incident projectiles is calculated. A sufficiently long Faraday cup is used in order to reduce the loss of backscattered electrons. Ejected electrons are detected using an electrostatic hemispherical analyzer combined with a channel electron multiplier (CEM) detector.

The electrodes of the analyzer are made up of oxygen-free high-conductivity (OFHC) copper hemispheres having radii of 2.5 cm and 3.5 cm, respectively. The electrodes are enclosed inside an OFHC copper housing. In order to suppress the production of secondary electrons from the electrodes, curved surfaces of the electrodes are coated with carbon soot. The trajectories of very-low-energy electrons (<5 eV) can be severely affected by the stray electric and magnetic fields present in the interaction region. A small preacceleration voltage of 6 V is applied to the entrance and the exit apertures of the spectrometer in order to have a better collection efficiency for these electrons. The entrance and the exit apertures have dimensions of  $4 \times 5 \text{ mm}^2$  and  $3 \times 5 \text{ mm}^2$ , respectively. Moreover, in order to reduce the effect of the Earth's magnetic field, two  $\mu$ -metal sheets are placed inside the chamber along the inner surface of the chamber. The energy resolution, which

depends mainly on the exit slit width and the acceptance angle of the entrance slit, is 6% of the electron energy. A voltage of +100 V is applied to the front of the CEM in order to achieve a uniform detection efficiency throughout the energy range. Electron yields are measured in the range from 1 to 330 eV (electron velocities between 0.3 and 4.9 a.u.). The background spectra are also recorded with no gas in the scattering chamber, and these spectra are subtracted from the CH<sub>4</sub> spectra.

## III. ANALYSIS OF THE SPECTRA

The DDCS of the electron emission at a given angle  $\theta$  is obtained from the measured electron spectrum by using the relation

$$\frac{d^2\sigma}{d\Omega dE} = \frac{N_e(E, \theta)/N_p - N_b(E, \theta)/N'_p}{\epsilon_{el} n (I\Omega)_{\text{eff}} \Delta\epsilon}, \quad (1)$$

where  $N_e$  and  $N_p$  are the number of detected electrons and the number of projectile ions, respectively. The quantities  $N_b$  and  $N'_p$  are the number of background counts recorded and the corresponding number of the incident ions, respectively. The  $\Delta\epsilon$  is the energy resolution of the spectrometer, and  $\epsilon_{el}$  is the detection efficiency of the CEM. It may be mentioned that the  $(I\Omega)_{\text{eff}}$  is the solid-angle path-length integral given by [53–56]

$$(I\Omega)_{\text{eff}} = \frac{w_1 w_2 h_2}{LR \sin\theta}, \quad (2)$$

where  $L$  is the length of the collimator in front of the analyzer entrance slit. The quantities  $w_1$  and  $h_1$  are the width and height of the entrance aperture of the collimator, respectively. The quantities  $w_2$  and  $h_2$  are the width and height of the exit aperture at the end of the collimator, respectively. The distance of the collimator from the center of the interaction zone [52,57] is denoted as  $R$ . The values of  $L$  and  $R$  are 36.5 mm and 59.5 mm, respectively. The values of the quantities  $w_1$ ,  $h_1$ ,  $w_2$ , and  $h_2$  are 3 mm, 4 mm, 2 mm, and 3 mm, respectively. The number density of the target gas at a pressure  $P_c$  is denoted by  $n = 9.659 \times 10^{15} P_c / T(K)$ , where  $P_c$  is in units of mTorr and  $T$  is the absolute temperature (in °K). The total error in the measurement mainly arises due to the uncertainties in the gas pressure ( $\sim 8\%–10\%$ ), detector efficiency ( $\sim 8\%–10\%$ ), solid angle ( $\sim 8\%–10\%$ ), and resolution ( $\sim 10\%–12\%$ ). The maximum statistical error is  $\sim 6\%$  for electrons of energy above 100 eV ejected in backward angles. The total uncertainty is thus about of  $\sim 20\%–25\%$ . However, the systematic errors due to stray fields may moderately increase it at lower energies, i.e., below 20 eV.

A small fraction of the lowest energy electrons may be lost before reaching the spectrometer due to the scattering in the target gas. However, the correction for this is estimated (from the known scattering cross sections) to be only about 5% for 5-eV electrons and is negligible at higher energies for light targets, such as H<sub>2</sub>, He, C, N<sub>2</sub>, O<sub>2</sub>, etc. In any case the data presented here is above 5 eV.

## IV. THEORETICAL TECHNIQUE

A single active electron model is employed, into an impact parameter formalism, in order to describe the single ionization

TABLE I. Population and binding energies of the CH<sub>4</sub> molecular orbitals.

MO	Population	Binding energy (a.u.)
C <sub>1s</sub>	2.0 C <sub>1s</sub>	-10.68
2a <sub>1</sub>	1.133 C <sub>2s</sub> + 0.867 H <sub>1s</sub>	-0.84
1t <sub>2</sub>	3.399 C <sub>2s</sub> + 2.601 H <sub>1s</sub>	-0.46

of the CH<sub>4</sub> molecule by the impact of bare carbon ions, assuming that the rest of the electrons remain frozen in their initial states [58]. It can be seen as a version for electron ionization of the one previously introduced for electron capture from molecular targets [59]. The influence of the interaction of the projectile on the molecular nuclei and with the passive electrons is reduced, in the impact parameter approximation, to an exponential factor which affects the projectile trajectory but does not contribute to the DDCS, which depend only on the angle and energy of the emitted electron [59,60]. The dynamics of the process is considered within the CDW-EIS approximation [58,61], which has been used with success to investigate the ionization of numerous atomic and molecular

targets under the interactions with ion beams. We should mention that a version of the CDW-EIS model has been applied to investigate ionization of CH<sub>4</sub> by proton impact [46].

The initial orbitals of the eight-electron molecular target in its fundamental state are represented using the complete neglect of differential overlaps (CNDO) approximation. Thus, each one of the orbital wave functions is described as a linear combination of the states of their atomic compounds. The corresponding binding energy is computed through a self-consistent field approximation (MO-LCAO-SCF). The populations and binding energies of the different orbitals are indicated in Table I [62]. In order to account for the long-range projectile field in the initial channel, distorted initial wave functions  $\chi_i^+$  are chosen, which are given by the expression

$$\chi_i^+ = \Phi_i L_i^+, \quad (3)$$

where  $\Phi_i$  are the orbital wave functions and  $L_i^+$  is the asymptotic eikonal projectile continuum phase. The supraindex (+) indicates that the distorted wave functions preserve correct outgoing asymptotic conditions.

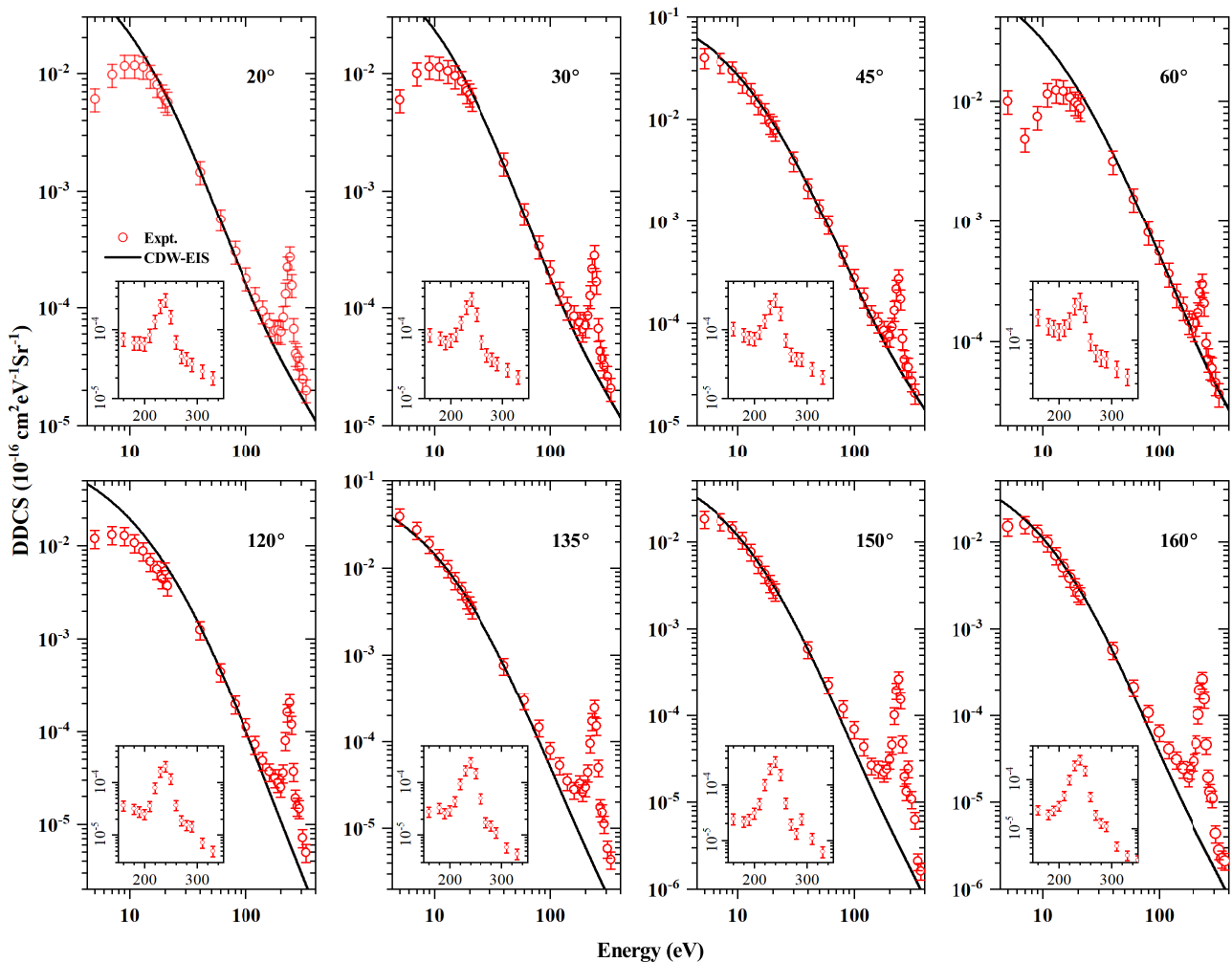


FIG. 1. Energy dependence of the ejected electron DDCS for CH<sub>4</sub> in collisions with 5.5 MeV/u bare C ions. The K-LL Auger electron peaks are shown in the insets.

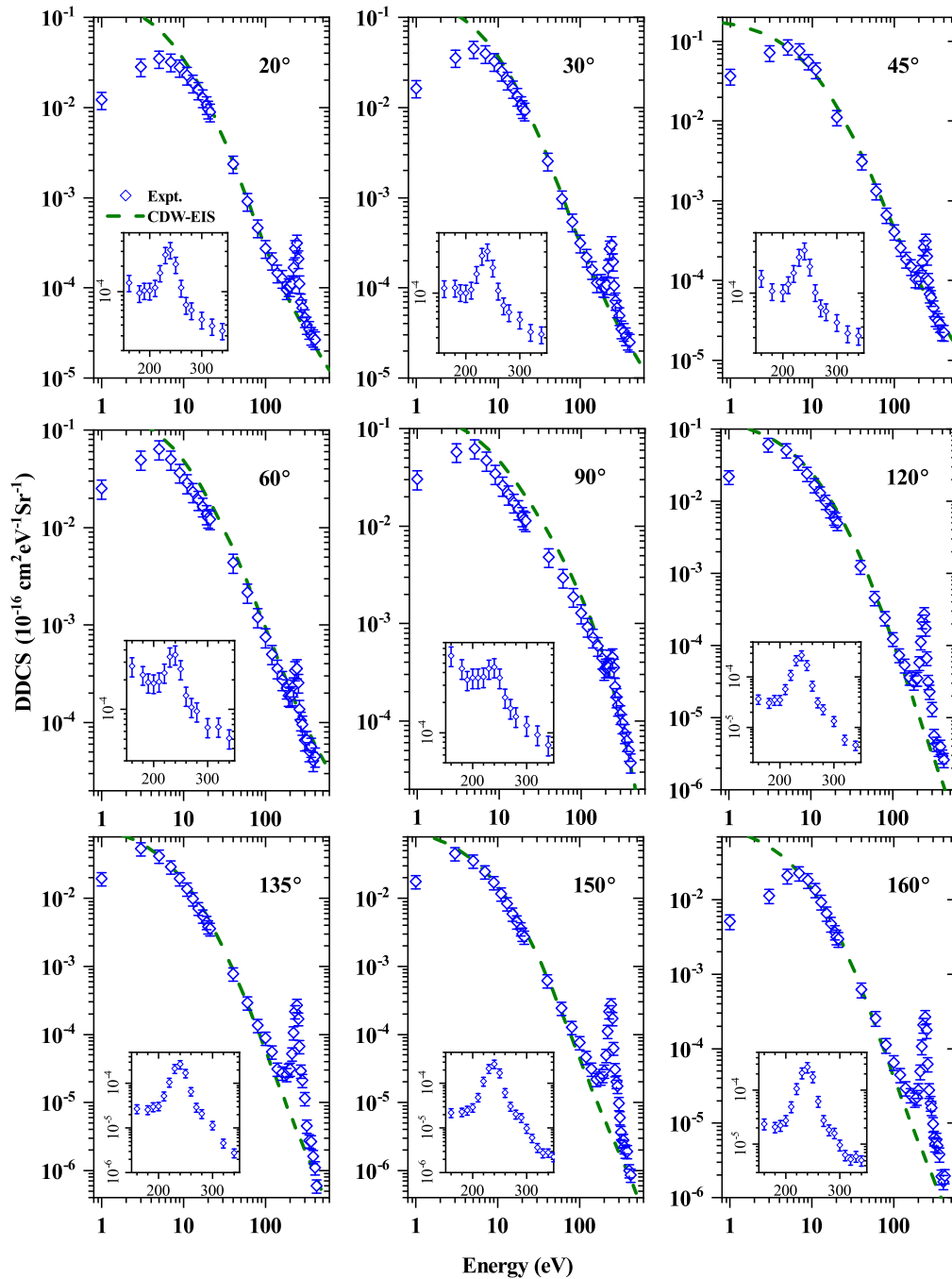


FIG. 2. Same as in Fig. 1 but for 3.5 MeV/u bare C ion projectiles.

In the exit channel, the target and projectile fields are considered to act simultaneously on equal footing on the ejected electron. Thus, the final distorted wave function  $\chi_f^-$  is chosen as

$$\chi_f^- = \Phi_f L_f^-, \quad (4)$$

$\Phi_f$  being continuum target wave functions corresponding to each one of the orbitals, which include the interaction of the active electron with the residual target, and  $L_f^-$  is the projectile Coulomb continuum factor that takes into account the interaction of the ejected electron with the bare projectile. The superscript (-) indicates that the wave function preserves

the correct incoming conditions. To simplify calculations, the target orbital wave functions  $\Phi_f$  are approximated by the Coulombic continuum ones with effective nuclear charges  $\zeta_T$ . They are obtained from the Belkić's prescription, where  $\zeta_T = n_i(-2\epsilon_f)^{1/2}$ ,  $\epsilon_f$  being the binding energy corresponding to each one of the molecular orbitals and  $n_i$  the principal quantum number of each one of the atomic wave function compounds. This prescription corresponds to approximate the target potential of the entry channel by an effective Coulombic one in the exit one.

The wave functions of the atomic compounds of the different orbitals are described within a Roothaan-Hartree-Fock

approximation [63], and the prior version of the CDW-EIS model is employed in the calculations. The transition amplitude corresponding to each orbital is written as [64,65]

$$A_{if}^-(\vec{\rho}) = -i \int_{-\infty}^{\infty} dt \langle \chi_f^- | (W_i | \chi_i^+) \rangle, \quad (5)$$

where  $\vec{\rho}$  is the impact parameter and  $W_i$  is the perturbative operator in the entry channel, so that

$$W_i \chi_i^+ = \frac{1}{2} \Phi_i \nabla^2 L_i^+ + \nabla \Phi_i \cdot \nabla L_i^+. \quad (6)$$

The scattering matrix element as a function of the transverse momentum transfer  $\vec{\eta}$  can be obtained by using the relation

$$R_{if}^-(\vec{\eta}) = \frac{1}{2\pi} \int d\vec{\rho} \exp(i\vec{\eta} \cdot \vec{\rho}) A_{if}^-(\vec{\rho}). \quad (7)$$

Doubly differential cross sections as a function of the solid angle and energy of the ejected electron are given by the expression

$$\frac{d^2\sigma}{d\Omega dE} = k \int d\vec{\eta} |R_{if}^-|^2, \quad (8)$$

where now all orbital contributions are added to obtain  $R_{if}^-$ . In Eq. (8),  $k$  indicates the momentum of the ejected electron with respect to the target.

## V. RESULTS AND DISCUSSION

### A. Double differential cross sections

#### 1. Energy distribution

The measured energy dependence of the e-DDCS is compared with those calculated using the CDW-EIS model in Figs. 1 and 2. All of the DDCS spectra show a rapid monotonic decrease with the increasing electron energy, except for the peaks appearing at  $\sim 240$  eV. These peaks correspond to the K-LL Auger electron emission from the C atom present in the CH<sub>4</sub> molecule. The spectra show large values of the DDCS in the low-energy range due to the dominance of the soft-collision process involving large impact parameters. The spectra fall off more than three orders of magnitude from 5 or 11 eV to 330 eV.

**5.5 MeV/u C<sup>6+</sup>.** Overall a very good agreement of the CDW-EIS model calculation with the measured values is observed for all the angles. The best agreement is found for the spectrum at 45° over the entire energy range. Among the other angles, very good agreement is observed for 20°, 30°, and 60° in the energy range from 20 eV to 180 eV. For energies <20 eV, the CDW-EIS model overestimates DDCS values at these angles. At the backward angles of 135°, 150°, and 160°, the CDW-EIS predictions are in agreement with the observed values up to the energy of 60 eV. However, the model underestimates the DDCS values with increasing energy beyond 60 eV. In the energy range from 120 eV to 180 eV, the CDW-EIS values are two-to-four times lower than the observed values. A similar trend is also observed at 120° for energies beyond 120 eV.

**3.5 MeV/u C<sup>6+</sup>.** A good agreement of the CDW-EIS model calculation with the measured values is observed for forward angles. For 20° and 30°, the CDW-EIS model

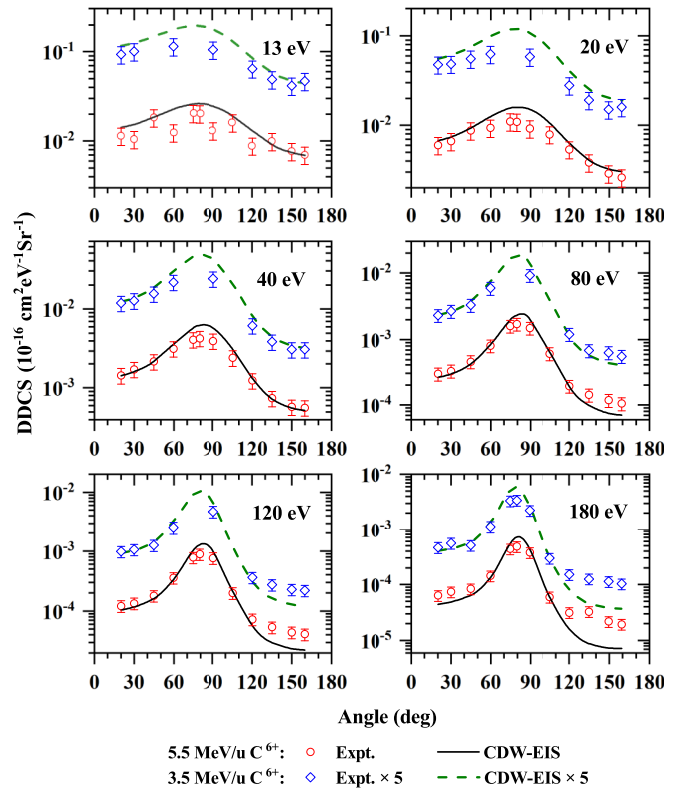


FIG. 3. The angular distribution of DDCS of electron emission from the CH<sub>4</sub> molecule in collisions with bare C ions. The observed and CDW-EIS values for 3.5 MeV/u projectiles are multiplied by a factor of 5.

overestimates the DDCS values below 20 eV, and the agreement becomes better with the increasing energy. For 60°, the predicted DDCS values are 1.2-to-1.5 times higher than the measured values. At the backward angles, the model underestimates the DDCS values above 80 eV, and the disagreement with the observed values increases with increasing energy. At these angles, the CDW-EIS underestimates the DDCS values by 40%–50% at energy around 160 eV.

The ratio of the DDCS (5 eV,  $\theta_i$ ) to DDCS (100 eV,  $\theta_i$ ) is almost the same for both projectiles for all values of emission angle,  $\theta_i$ . The DDCS spectrum for a given  $\theta_i$  has almost the same slope in this energy range, i.e., from 5 eV to 100 eV, for both projectiles. At higher projectile energy the cross section is smaller, as also predicted by the perturbative calculations.

The underestimation of the electron emission cross section at high electron energies for 5.5 and 3.3 MeV/u could have their origin in the fact that backscattering at high emission energies is expected to be produced mainly in the proximity of the C nucleus, where the orbital electrons have high velocity. The projectile collides on the electron such that the electron is deviated onto the target nucleus and then suffers an elastic scattering which reorients the ejected electron in the backward direction [66]. Thus, for the C<sub>1s</sub> contribution a charge  $\zeta_T = 6$  is chosen for  $L_f^-$  in Eq. (4).

The fall in the experimental DDCS values towards low electron energies at some angles for both projectile energies (cf. Figs. 1 and 2) is due to the existence of stray magnetic and electric fields affecting the trajectories of these low-energy

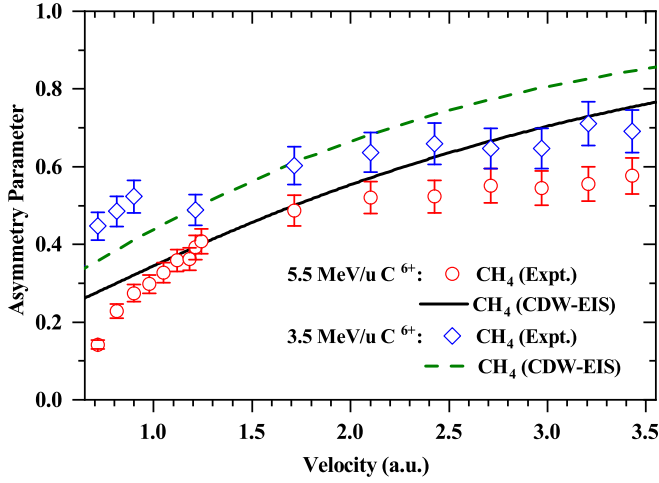


FIG. 4. Asymmetry parameter as a function of ejected electron velocity,  $k$ .

electrons. Despite taking steps to reduce the effect of electric and magnetic fields as discussed in Sec. II, their effect can be observed in the DDCS spectra at low energies.

## 2. Angular distribution

The angular distributions of the electron DDCS at six different energies are shown in Fig. 3. The overall shape of the spectrum is correctly predicted by the CDW-EIS model for both projectile energies.

**5.5 MeV/u  $C^{6+}$ .** The emission is almost isotropic for the lowest energy electrons, such as for 13 eV with a humplike feature around  $\sim 90^\circ$ , which is well known for the soft-collision mechanism. At energies of 20 eV and 40 eV, the CDW-EIS calculations are in agreement for the forward angles  $20^\circ$ ,  $30^\circ$ , and  $45^\circ$  and backward angles  $135^\circ$ ,  $150^\circ$ , and  $160^\circ$ . For angles of  $60^\circ$ - $105^\circ$ , the model overestimates the DDCS values with maximum discrepancy at  $90^\circ$ , where the calculated values are  $\sim 1.5$  times higher than the observed ones. At energies 80 eV, 120 eV, and 180 eV, the CDW-EIS values are in agreement at lower forward angles. However, the model calculation underestimates the DDCS values at higher backward angles. For instance, at 120 eV the predicted DDCS values are  $\sim 50\%$  of the observed ones at angles  $135^\circ$ ,  $150^\circ$ , and  $160^\circ$ .

**3.5 MeV/u  $C^{6+}$ .** At the energy of 20 eV, the CDW-EIS calculations are in agreement at extreme forward and backward angles. At angles in between, the DDCS values predicted by model calculations are higher than the observed ones with maximum discrepancy at  $90^\circ$  where the CDW-EIS value is 1.6 times higher than the observed one. A similar trend is also observed at 40 eV. The predicted angular distributions at 80 eV, 120 eV, and 180 eV are in agreement with the observed values except at the extreme backward angles. At these angles, the model predictions are lower than the observed values by  $\sim 40\%$ ,  $\sim 50\%$ , and  $\sim 70\%$  at 80 eV, 120 eV, and 180 eV, respectively. For higher emission energies, the large yield at backward angles could be due to a backscattering mechanism discussed in the previous section.

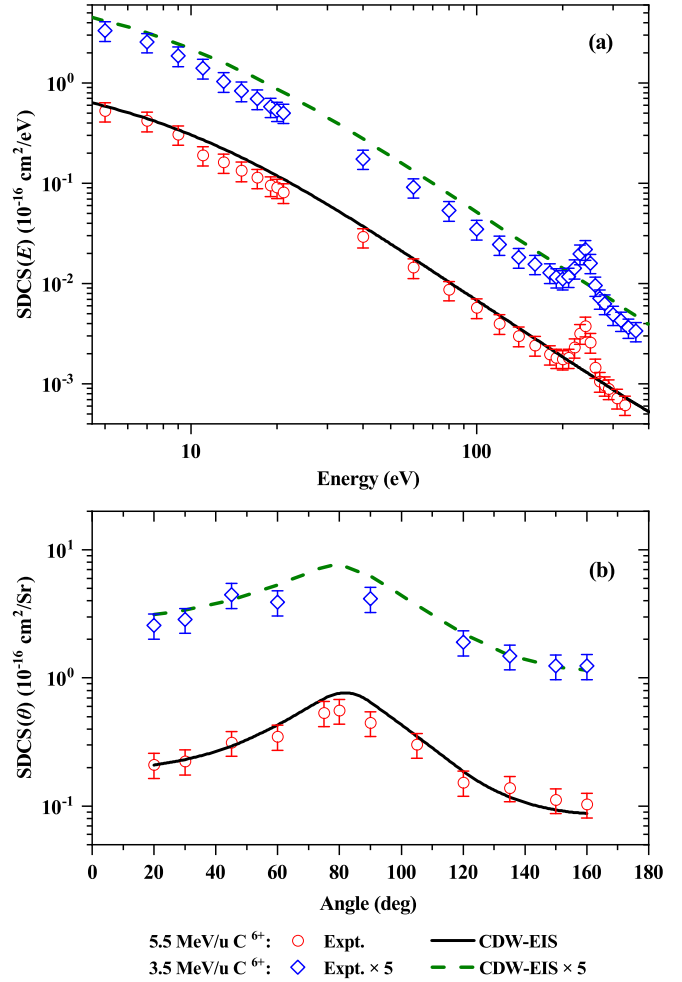


FIG. 5. (a) Energy and (b) angle dependence of SDCS of electron emission. The measured and the CDW-EIS values for 3.5 – MeV/u projectiles are multiplied by a factor of 5.

The peaklike shape in the angular distributions at both projectile energies becomes more prominent with increasing emitted electron energy, and at higher energies the peak becomes sharper at around  $80^\circ$ . This feature is well known in ion-atom collisions and is a signature of the binary nature of the collision [67]. When a free electron initially at rest collides with a fast projectile ion, the target electron is deflected in a particular direction for any amount of energy transfer, and this results in a  $\delta$ -function peak in the angular distribution. Since the target electrons are bound, they have an initial momentum distribution which causes the observed broadening of the  $\delta$ -function-type angular distribution. The peak position  $\theta_{BE}$  of the  $\delta$  function in the angular distribution is given by  $\cos^2 \theta_{BE} = v_e^2/v_p^2$ , where  $v_e$  and  $v_p$  are the velocities of the ejected electron and the projectile ion, respectively [68]. For an emission energy of 120 eV and projectile energy of 5.5 MeV/u, this classical formula predicts the peak at  $83^\circ$ , which matches very well with the observed position.

It can also be noticed that cross sections at the forward angles are higher than those at corresponding complementary backward angles, and this forward-backward angular asymmetry increases with increasing electron energy. One of the

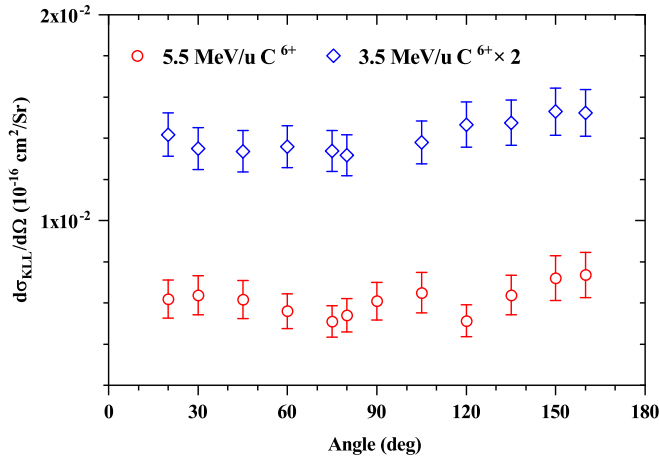


FIG. 6. Angular dependence of carbon K-LL Auger emission cross section. The values for 3.5-MeV/u projectiles are multiplied by a factor of 2. Only relative errors are shown. Absolute errors are about 20%–25%.

reasons for such asymmetry is the two-center effect in which the ejected electrons are affected by the Coulomb fields of both the target nucleus and the projectile ion. The emission of the electrons in forward angles is enhanced due to the strong attraction by the projectiles moving in the same direction. The electrons of very low energies are not affected by this effect, since their velocities are very small compared to the projectile velocity. The forward-backward angular asymmetry can be quantified by defining a quantity  $\alpha(k, \theta)$  known as the asymmetry parameter,

$$\alpha(k, \theta) = \frac{\sigma(k, \theta) - \sigma(k, \pi - \theta)}{\sigma(k, \theta) + \sigma(k, \pi - \theta)}, \quad (9)$$

where  $k$  is the electron velocity in a. u. (ejected electron energy,  $\epsilon_k = k^2/2$ , in a. u.) and  $\theta$  is the forward angle. In the present case,  $\theta = 45^\circ$  is used to calculate the forward-backward angular asymmetry. For 5.5-MeV/u projectiles, the asymmetry parameter rises sharply from a value of 0.14 at  $k \sim 0.72$  a.u. to 0.49 at 1.71 a. u. (cf. Fig. 4). Then a saturating trend is observed for  $k$  beyond 2.1 a. u. In the case of 3.5-MeV/u projectiles, although the sharp rise in the lower velocities is not observed, the saturating trend is observed beyond 2.1 a. u. The CDW-EIS does not predict this saturating trend and overestimates the asymmetry parameter values at higher values of  $k$ . The asymmetry parameter for projectiles with lower energy, i.e., 3.5 MeV/u, is higher than that for higher energy by  $\sim 20\%$  at higher values of  $k$ . This is consistent with the CDW-EIS model calculations and implies a stronger

manifestation of the TCE for the lower energy (3.5 MeV/u) ions than in the case of higher energy (5.5 MeV/u) projectiles.

### B. Single differential cross sections and the total cross section

The single differential cross sections are calculated from the DDCS values by integrating them over the electron energy and the emission angle, i.e.,

$$\text{SDCS}(\theta) = \frac{d\sigma}{d\Omega} = \int_{E_i}^{E_f} \frac{d^2\sigma}{d\Omega dE} dE, \quad (10a)$$

$$\text{SDCS}(E) = \frac{d\sigma}{dE} = 2\pi \int_{\theta_i}^{\theta_f} \frac{d^2\sigma}{d\Omega dE} \sin\theta d\theta, \quad (10b)$$

where the angular range is from  $20^\circ$  to  $160^\circ$ . The energy range is from 11 eV to 330 eV for 5.5-MeV/u projectiles and from 5 eV to 330 eV for 3.5-MeV/u projectiles. The  $\text{SDCS}(E)$  and the  $\text{SDCS}(\theta)$  values are plotted in Figs. 5(a) and 5(b), respectively. The overall shapes of both  $\text{SDCS}(E)$  and  $\text{SDCS}(\theta)$  are well predicted by the CDW-EIS model. The  $\text{SDCS}(E)$  values predicted by the CDW-EIS model are 1.2–1.4 times higher for 5.5-MeV/u projectiles and 1.2–1.6 times higher for 3.5 MeV/u projectiles as compared to the measured values. In the case of  $\text{SDCS}(\theta)$ , the agreement is good at angles of  $20^\circ$ ,  $30^\circ$ , and  $45^\circ$  and their complementary backward angles for both projectile energies. However, the CDW-EIS values are 1.3–1.4 times higher at angles of  $75^\circ$ ,  $80^\circ$ , and  $90^\circ$ .

The angle dependence of the C K-LL Auger emission cross section  $d\sigma_{\text{KLL}}/d\Omega$  is also calculated by integrating the peak at  $\sim 240$  eV after subtracting the continuum electron background for each angle (cf. Fig. 6). The Auger electron emission is found to be almost isotropic for both projectile energies. There is a slight variation in these values between 0.5 and  $0.8 (\times 10^{-16})$  for the higher energy collisions. A similar slight variation is also seen in the case of the projectile with energy 3.5 MeV/u. A purely isotropic distribution is expected in the case of an atomic target.

The total cross-section (TCS) of electron emission is obtained by integrating the  $\text{SDCS}(\theta)$  over the electron emission angles or by integrating  $\text{SDCS}(E)$  over the emitted electron energies, i.e.,

$$\text{TCS} = 2\pi \int_{\theta_i}^{\theta_f} \frac{d\sigma}{d\Omega} \sin\theta d\theta = \int_{E_i}^{E_f} \frac{d\sigma}{dE} dE. \quad (11)$$

The TCS is mostly contributed by the low-energy electrons produced by soft collisions. In the derivation of the TCS, the angular range from  $20^\circ$  to  $160^\circ$  is considered. For 5.5 MeV/u projectiles, the experimental DDCS data show a fall below the electron energy of 5 or 10 eV at some angles. Taking the

TABLE II. The TCS of electron emission and the carbon K-LL Auger electron emission cross section ( $\sigma_{\text{KLL}}$ ). The TCS values derived by integrating between 5 and 330 eV are shown. For reference the “overall CDW-EIS” prediction, i.e., integrated over all energies (0 to  $\infty$ ) and angles, is also shown. The values are in  $\text{cm}^2$ , and the uncertainty in measurements is  $\sim 20\% - 25\%$ .

$E_p$ (MeV/u)	Expt. (5–330 eV)	CDW-EIS (5–330 eV)	Ratio (5–330 eV) (Expt./CDW-EIS)	CDW-EIS (Overall)	$\sigma_{\text{KLL}}$ (Expt.)
3.5	$7.31 \times 10^{-16}$	$9.93 \times 10^{-16}$	0.74	$1.74 \times 10^{-15}$	$9.25 \times 10^{-18}$
5.5	$5.81 \times 10^{-16}$	$6.78 \times 10^{-16}$	0.85	$1.19 \times 10^{-15}$	$8.03 \times 10^{-18}$

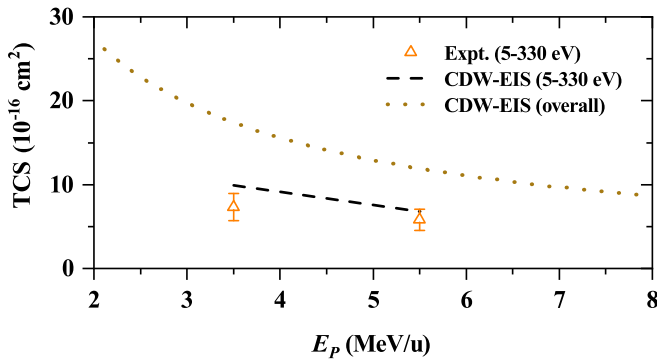


FIG. 7. The TCS as a function of  $\text{C}^{6+}$  projectile energy  $E_p$ .

energy range 5 eV to 330 eV, the experimental TCS value is found to be  $5.81 \times 10^{-16} \text{ cm}^2$ , whereas a value of  $6.78 \times 10^{-16} \text{ cm}^2$  is obtained from the model calculation. Thereby the experiment-to-theory ratio is 0.85. For 3.5-MeV/u projectiles, considering the same energy range, the experimental and theoretical TCS are found to be  $7.31 \times 10^{-16} \text{ cm}^2$  and  $9.93 \times 10^{-16} \text{ cm}^2$ , respectively, giving the experiment-to-theory ratio of 0.74.

In order to consider the contribution to the TCS, due to the electrons of lowest energy for which the experimental data are not available, the experimental SDSCS data are extrapolated in low energies up to 1 eV by following the slope provided by the CDW-EIS. The TCS value in the energy range from 1 eV to 330 eV do not include the contribution from angles below  $20^\circ$  and above  $160^\circ$ . It is found, from the CDW-EIS calculation, that the contribution of the angles below  $20^\circ$  and above  $160^\circ$  to the TCS is  $\sim 7\%$  for 3.5-MeV projectiles and  $\sim 4\%$  for 5.5-MeV projectiles. A similar percentage contribution from these missing angles can be expected to the measured TCS. These contributions are included in the derived TCS displayed in Table II. The measured TCS values (between 5 and 330 eV) are plotted along with the CDW-EIS prediction (dashed line) in Fig. 7. The predictions are higher than the measured values by about 35% and 17% for 3.5-MeV/u and 5.5-MeV/u projectiles, respectively. Also, the dotted line displays the “overall TCS” as predicted by the CDW-EIS, obtained by integrating over all the energies (0 to  $\infty$ ) and all the angles, which is provided as a reference.

The total C K-LL Auger electron emission cross section  $\sigma_{\text{KLL}}$  is also calculated by integrating  $d\sigma_{\text{KLL}}/d\Omega$  over emission angles from  $0^\circ$  to  $180^\circ$  (cf. Table II). The K-LL Auger electrons arise due to the K-shell ionization and the K-shell electron transfer to the projectile vacant states. Considering the flat nature of the  $d\sigma_{\text{KLL}}/d\Omega$  for small forward and largest backward angles, the values at  $0^\circ$  and  $180^\circ$  are determined by extrapolation, in order to derive  $\sigma_{\text{KLL}}$ . One may also find the indication of the hypersatellite peak beyond the KLL Auger peak, which arises due to double K vacancy in such heavy-ion collisions. The signature of this peak is visible at extreme backward angles.

## VI. CONCLUSIONS

The absolute DDSCS of electron emission from a  $\text{CH}_4$  molecule induced by 3.5 MeV/u and 5.5 MeV/u bare C ions are measured in the emission energy ranges 11–330 eV and 5–330 eV, respectively. The range of emission angle was chosen from  $20^\circ$  to  $160^\circ$ . The results are compared with the prior version of the CDW-EIS model calculation along with the CNDO approach to describe the target molecule. A very good overall agreement is found between the observed values and those calculated from the CDW-EIS model at most of the energies and angles, except for the highest energy electrons emitted in extreme backward angles. Nevertheless, the overall good agreement of the theoretical model with the experimental measurements provides confidence to extend such calculations for larger molecules. A stronger effect of the TCE, through the measurement of the forward-backward angular asymmetry, is observed for the lower energy projectile as compared to higher energy. The single differential cross sections (SDSCS) and the total cross section (TCS) are deduced from the DDSCS values. The C K-LL Auger electron emission is found to be isotropic, thus, displaying an atomlike behavior. The total Auger emission cross section is also deduced, which provides the total K-vacancy production cross section.

## ACKNOWLEDGMENTS

The authors thank the staff members of the Pelletron Accelerator facility at TIFR for the smooth operation of the machine, and Nilesh Mhatre and Sadashiv Manjrekar for their help during the experiment.

- [1] L. C. Tribedi, P. Richard, Y. D. Wang, C. D. Lin, and R. E. Olson, *Phys. Rev. Lett.* **77**, 3767 (1996).
- [2] N. Stolterfoht, B. Sulik, V. Hoffmann, B. Skogvall, J. Y. Chesnel, J. Rangama, F. Frémont, D. Hennecart, A. Cassimi, X. Husson, A. L. Landers, J. A. Tanis, M. E. Galassi, and R. D. Rivarola, *Phys. Rev. Lett.* **87**, 023201 (2001).
- [3] D. Misra, U. Kadhane, Y. P. Singh, L. C. Tribedi, P. D. Fainstein, and P. Richard, *Phys. Rev. Lett.* **92**, 153201 (2004).
- [4] F. Frémont, A. Hajaji, A. Naja, C. Leclercq, J. Soret, J. A. Tanis, B. Sulik, and J. Y. Chesnel, *Phys. Rev. A* **72**, 050704(R) (2005).
- [5] D. Misra, A. Kelkar, U. Kadhane, A. Kumar, L. C. Tribedi, and P. D. Fainstein, *Phys. Rev. A* **74**, 060701(R) (2006).
- [6] N. Stolterfoht, H. Platten, G. Schiwietz, D. Schneider, L. Gulyás, P. D. Fainstein, and A. Salin, *Phys. Rev. A* **52**, 3796 (1995).
- [7] D. Misra, A. H. Kelkar, P. D. Fainstein, and L. C. Tribedi, *J. Phys. B: At. Mol. Opt. Phys.* **45**, 225201 (2012).
- [8] A. N. Agnihotri, S. Nandi, S. Kasthurirangan, A. Kumar, M. E. Galassi, R. D. Rivarola, C. Champion, and L. C. Tribedi, *Phys. Rev. A* **87**, 032716 (2013).
- [9] L. C. Tribedi, M. Roy Chowdhury, S. Bhattacharjee, C. Bagdia, A. Mandal, D. Misra, C. Champion, J. Monti, and R. Rivarola, *J. Phys. Conf. Ser.* **875**, 102011 (2017).
- [10] P. Moretto-Capelle and A. Le Padellec, *Phys. Rev. A* **74**, 062705 (2006).
- [11] P. de Vera, R. Garcia-Molina, and I. Abril, *Phys. Rev. Lett.* **114**, 018101 (2015).



- [12] L. J. Allamandola, D. M. Hudgins, and S. A. Sandford, *Astrophys. J.* **511**, L115 (1999).
- [13] F. Y. Xiang, A. Li, and J. X. Zhong, *Astrophys. J.* **733**, 91 (2011).
- [14] E. L. O. Bakes and A. G. G. M. Tielens, *Astrophys. J.* **499**, 258 (1998).
- [15] A. G. G. M. Tielens, *Rev. Mod. Phys.* **85**, 1021 (2013).
- [16] A. Leger and L. D'Hendecourt, *Astron. Astrophys.* **146**, 81 (1985).
- [17] S. Biswas and L. C. Tribedi, *Phys. Rev. A* **92**, 060701(R) (2015).
- [18] S. Biswas, C. Champion, P. F. Weck, and L. C. Tribedi, *Sci. Rep.* **7**, 17131 (2017).
- [19] U. Kadhane, A. Kelkar, D. Misra, A. Kumar, and L. C. Tribedi, *Phys. Rev. A* **75**, 041201(R) (2007).
- [20] I. V. Hertel, H. Steger, J. de Vries, B. Weisser, C. Menzel, B. Kamke, and W. Kamke, *Phys. Rev. Lett.* **68**, 784 (1992).
- [21] S. W. J. Scully, E. D. Emmons, M. F. Gharaibeh, R. A. Phaneuf, A. L. D. Kilcoyne, A. S. Schlachter, S. Schippers, A. Müller, H. S. Chakraborty, M. E. Madjet, and J. M. Rost, *Phys. Rev. Lett.* **94**, 065503 (2005).
- [22] T. LeBrun, H. G. Berry, S. Cheng, R. W. Dunford, H. Esbensen, D. S. Gemmell, E. P. Kanter, and W. Bauer, *Phys. Rev. Lett.* **72**, 3965 (1994).
- [23] H. Tsuchida, A. Itoh, K. Miyabe, Y. Bitoh, and N. Imanishi, *J. Phys. B: At. Mol. Opt. Phys.* **32**, 5289 (1999).
- [24] V. Formisano, S. Atreya, T. Encrenaz, N. Ignatiev, and M. Giuranna, *Science* **306**, 1758 (2004).
- [25] D. W. Koopman, *J. Chem. Phys.* **49**, 5203 (1968).
- [26] K. H. Berkner, R. V. Pyle, and J. W. Stearns, *Nucl. Fusion* **10**, 145 (1970).
- [27] R. J. McNeal, *J. Chem. Phys.* **53**, 4308 (1970).
- [28] M. Eliot, *J. Phys.* **38**, 21 (1977).
- [29] B. G. Lindsay, W. S. Yu, and R. F. Stebbings, *J. Phys. B: At. Mol. Opt. Phys.* **38**, 1977 (2005).
- [30] T. Kusakabe, K. Asahina, A. Iida, Y. Tanaka, Y. Li, G. Hirsch, R. J. Buenker, M. Kimura, H. Tawara, and Y. Nakai, *Phys. Rev. A* **62**, 062715 (2000).
- [31] B. E. Fuentes, J. López-Patiño, F. B. Yousif, and H. Martínez, *Int. J. Mass Spectrom.* **411**, 21 (2016).
- [32] J. G. Collins and P. Kebarle, *J. Chem. Phys.* **46**, 1082 (1967).
- [33] L. H. Toburen, M. Y. Nakai, and R. A. Langley, *Phys. Rev.* **171**, 114 (1968).
- [34] M. E. Rudd, R. D. Dubois, L. H. Toburen, C. A. Ratcliffe, and T. V. Goffe, *Phys. Rev. A* **28**, 3244 (1983).
- [35] R. S. Gao, L. K. Johnson, C. L. Hakes, K. A. Smith, and R. F. Stebbings, *Phys. Rev. A* **41**, 5929 (1990).
- [36] R. Browning and H. B. Gilbody, *J. Phys. B: At. Mol. Phys.* **1**, 1149 (1968).
- [37] I. Ben-Itzhak, K. D. Carnes, S. G. Ginther, D. T. Johnson, P. J. Norris, and O. L. Weaver, *Phys. Rev. A* **47**, 3748 (1993).
- [38] I. Ben-Itzhak, K. D. Carnes, D. T. Johnson, P. J. Norris, and O. L. Weaver, *Phys. Rev. A* **49**, 881 (1994).
- [39] H. Luna, E. G. Cavalcanti, J. Nickles, G. M. Sigaud, and E. C. Montenegro, *J. Phys. B: At. Mol. Opt. Phys.* **36**, 4717 (2003).
- [40] H. Knudsen, U. Mikkelsen, K. Paludan, K. Kirsebom, S. P. Møller, E. Uggerhøj, J. Slevin, M. Charlton, and E. Morenzoni, *J. Phys. B: At. Mol. Opt. Phys.* **28**, 3569 (1995).
- [41] N. B. Malhi, I. Ben-Itzhak, T. J. Gray, J. C. Legg, V. Needham, K. Carnes, and J. H. McGuire, *J. Chem. Phys.* **87**, 6502 (1987).
- [42] M. Dogan, M. Ulu, Z. N. Ozer, M. Yavuz, and G. Bozkurt, *J. Spectrosc.* **2013**, 192917 (2013).
- [43] W. E. Wilson and L. H. Toburen, *Phys. Rev. A* **11**, 1303 (1975).
- [44] L. Gulyás, I. Tóth, and L. Nagy, *J. Phys. B: At. Mol. Opt. Phys.* **46**, 075201 (2013).
- [45] A. Mondal, S. Halder, S. Mukherjee, C. R. Mandal, and M. Purkait, *Phys. Rev. A* **96**, 032710 (2017).
- [46] S. T. S. Kovács, P. Herczku, Z. Juhász, L. Sarkadi, L. Gulyás, and B. Sulik, *Phys. Rev. A* **94**, 012704 (2016).
- [47] D. Misra, A. Kelkar, U. Kadhane, A. Kumar, Y. P. Singh, L. C. Tribedi, and P. D. Fainstein, *Phys. Rev. A* **75**, 052712 (2007).
- [48] L. C. Tribedi, P. Richard, W. DeHaven, L. Gulyás, M. W. Gealy, and M. E. Rudd, *J. Phys. B: At. Mol. Opt. Phys.* **31**, L369 (1998).
- [49] L. C. Tribedi, P. Richard, L. Gulyás, and M. E. Rudd, *Phys. Rev. A* **63**, 062724 (2001).
- [50] L. C. Tribedi, P. Richard, L. Gulyás, M. E. Rudd, and R. Moshhammer, *Phys. Rev. A* **63**, 062723 (2001).
- [51] P. D. Fainstein, L. Gulyás, F. Martín, and A. Salin, *Phys. Rev. A* **53**, 3243 (1996).
- [52] D. Misra, K. V. Thulasiram, W. Fernandes, A. H. Kelkar, U. Kadhane, A. Kumar, Y. Singh, L. Gulyás, and L. C. Tribedi, *Nucl. Instrum. Methods Phys. Res., Sect. B* **267**, 157 (2009).
- [53] C. E. Kuyatt, in *Methods of Experimental Physics*, edited by L. Marton (Academic Press, New York, 1968), Vol. 7A, Chap. 1, p. 13.
- [54] E. B. Jordan and R. B. Brode, *Phys. Rev.* **43**, 112 (1933).
- [55] R. G. Herb, D. W. Kerst, D. B. Parkinson, and G. J. Plain, *Phys. Rev.* **55**, 998 (1939).
- [56] M. W. Gealy, G. W. Kerby, Y.-Y. Hsu, and M. E. Rudd, *Phys. Rev. A* **51**, 2247 (1995).
- [57] G. Scoles, *Atomic and Molecular Beam Methods* (Oxford University Press, New York, 1988), Chap. 4, pp. 83–90.
- [58] P. D. Fainstein, V. H. Ponce, and R. D. Rivarola, *J. Phys. B: At. Mol. Opt. Phys.* **21**, 287 (1988).
- [59] S. E. Corchs, R. D. Rivarola, and J. H. McGuire, *Phys. Rev. A* **47**, 3937 (1993).
- [60] M. F. Ciappina, O. A. Fojón, and R. D. Rivarola, *J. Phys. B: At. Mol. Opt. Phys.* **47**, 042001 (2014).
- [61] D. S. F. Crothers and J. F. McCann, *J. Phys. B: At. Mol. Opt. Phys.* **16**, 3229 (1983).
- [62] R. Hoffmann, *J. Chem. Phys.* **39**, 1397 (1963).
- [63] E. Clementi and C. Roetti, *At. Data Nucl. Data Tables* **14**, 177 (1974).
- [64] P. D. Fainstein, V. H. Ponce, and R. D. Rivarola, *J. Phys. B: At. Mol. Opt. Phys.* **24**, 3091 (1991).
- [65] J. M. Montí, O. A. Fojón, J. Hanssen, and R. D. Rivarola, *J. Phys. B: At. Mol. Opt. Phys.* **43**, 205203 (2010).
- [66] N. Stolterfoht, R. D. DuBois, and R. D. Rivarola, *Electron Emission in Heavy Ion-Atom Collisions*, Springer Series on Atomic, Optical, and Plasma Physics Vol. 20 (Springer, Berlin, 1997).
- [67] S. T. Manson, L. H. Toburen, D. H. Madison, and N. Stolterfoht, *Phys. Rev. A* **12**, 60 (1975).
- [68] T. Bonsen and L. Vriens, *Physica* **47**, 307 (1970).

*Correction:* Text directly preceding Sec. IV and at the end of the penultimate paragraph of Sec. V was inadvertently removed during production and has been reinserted.